Journal of Luminescence 209 (2019) 302–315

Contents lists available at ScienceDirect

Journal of Luminescence

journal homepage: www.elsevier.com/locate/jlumin

Roles of oxygen vacancies and pH induced size changes on photo- and radioluminescence of undoped and Eu^{3+}-doped $La_2Zr_2O_7$ nanoparticles

Santosh K. Gupta[a,b], Maya Abdou[a], Jose P. Zuniga[a], Partha S. Ghosh[c], Enrique Molina[d], Ben Xu[d], Mircea Chipara[e], Yuanbing Mao[a,f,*]

[a] Department of Chemistry, University of Texas Rio Grande Valley, 1201 West University Drive, Edinburg, TX 78539, USA
[b] Radiochemistry Division, Bhabha Atomic Research Centre, Trombay, Mumbai 400085, India
[c] Materials Science Division, Bhabha Atomic Research Centre, Trombay, Mumbai 400085, India
[d] Department of Mechanical Engineering, University of Texas Rio Grande Valley, 1201 West University Drive, Edinburg, TX 78539, USA
[e] Department of Physics and Astronomy, University of Texas Rio Grande Valley, 1201 West University Drive, Edinburg, TX 78539, USA
[f] School of Earth, Environmental, and Marine Sciences, University of Texas Rio Grande Valley, 1201 West University Drive, Edinburg, TX 78539, USA

ARTICLE INFO

Keywords:
$La_2Zr_2O_7$
Photoluminescence
Radioluminescence
Europium
Nanoparticles

ABSTRACT

Defect, doping and particle size play important roles on the optical performance of nanophosphors. In this study, undoped $La_2Zr_2O_7$ NPs (LZO) displayed multicolor emission under UV irradiation due to the presence of ionized oxygen vacancies in the band gap. In addition, we explored the effect of particle size of $La_2Zr_2O_7$:Eu^{3+} (LZOE) NPs on their structure, surface area, photoluminescence, radioluminescence, lifetime and quantum yield. There is progressive decrease in luminescence output and quantum yield as the coprecipitation pH is raised to prepare the single-source precursors for the molten salt synthesis of the NPs. Under X-ray irradiation, the LZOE NPs emit red light highlighting their potential as X-ray scintillator. We explained the experimental observations based on surface defect analogy. The experimentally obtained emission in violet-blue and red optical regions is correlated to defect related emission. High asymmetry ratio suggested low symmetric environment of Eu^{3+} ions in the LZO host and the occupancy of Eu^{3+} ions is more favorable at LaO_8 site compared to ZrO_6 site. Emission spectra of the LZOE also showed favorable host to dopant (Eu^{3+}) energy transfer. This work provides a clear picture of making highly efficient red phosphor and X-ray scintillator for applications in optoelectronics and X-ray induced theranostics.

1. Introduction

Materials with $A_2B_2O_7$ (A is trivalent ions, B is tetravalent ions, and O is oxygen) composition have been studied extensively in last few decades due to their interesting properties such as low thermal conductivity, high radiation stability, high refractive index, high mechanical strength, and high thermal stability [1–5]. These properties make them suitable for various interesting applications such as thermal barrier coatings [6], magnets [7,8], catalysts [9,10], sensors [11], optical materials [12], solid-oxide fuel cells [13], and nuclear waste hosts [14], etc. Usually, phosphors prepared by high temperature solid-state route have micron-sized particles which are not desirable for optoelectronics, scintillator and x-ray based bioimaging applications. In recent years, molten salt synthesis (MSS) technique has been regarded as an effective and convenient method to synthesize nanoparticles at relatively low temperature with high level of monodispersity. Moreover, pyrochlore nanoparticles (NPs) have recently gained significant attention compared to their bulk counterparts in areas of solid oxide fuel cells [15,16], photocatalysis [17,18], thermographic phosphor [19], thermal barrier coatings [20], radiation detector [5,21], nuclear waste host [22], photoluminescence [23–26], scintillation [24–26], and magnetism [27], etc. $La_2Zr_2O_7$ in that context has been one of the standout pyrochlores for its suitability in various kinds of technological applications such as luminescence, scintillator, ferroelectric material, nuclear waste host, photoelectrochemical catalyst, and electrode material in fuel cell, etc. [14,24,28–30]. As a host for lanthanide doped nanophosphors, $La_2Zr_2O_7$ has several favorable properties such as high thermal stability, ability to accommodate dopant ions at both A and B sites, having rugged structure and high radiation stability. For such reasons, it has been predominately used as a host for doped inorganic phosphors [24,31–35].

Doping nanoparticles is an efficient way to synthesize tunable

* Corresponding author at: Department of Chemistry, University of Texas Rio Grande Valley, 1201 West University Drive, Edinburg, TX 78539, USA.
E-mail address: yuanbing.mao@utrgv.edu (Y. Mao).

https://doi.org/10.1016/j.jlumin.2019.01.059
Received 16 October 2018; Received in revised form 30 January 2019; Accepted 31 January 2019
Available online 01 February 2019

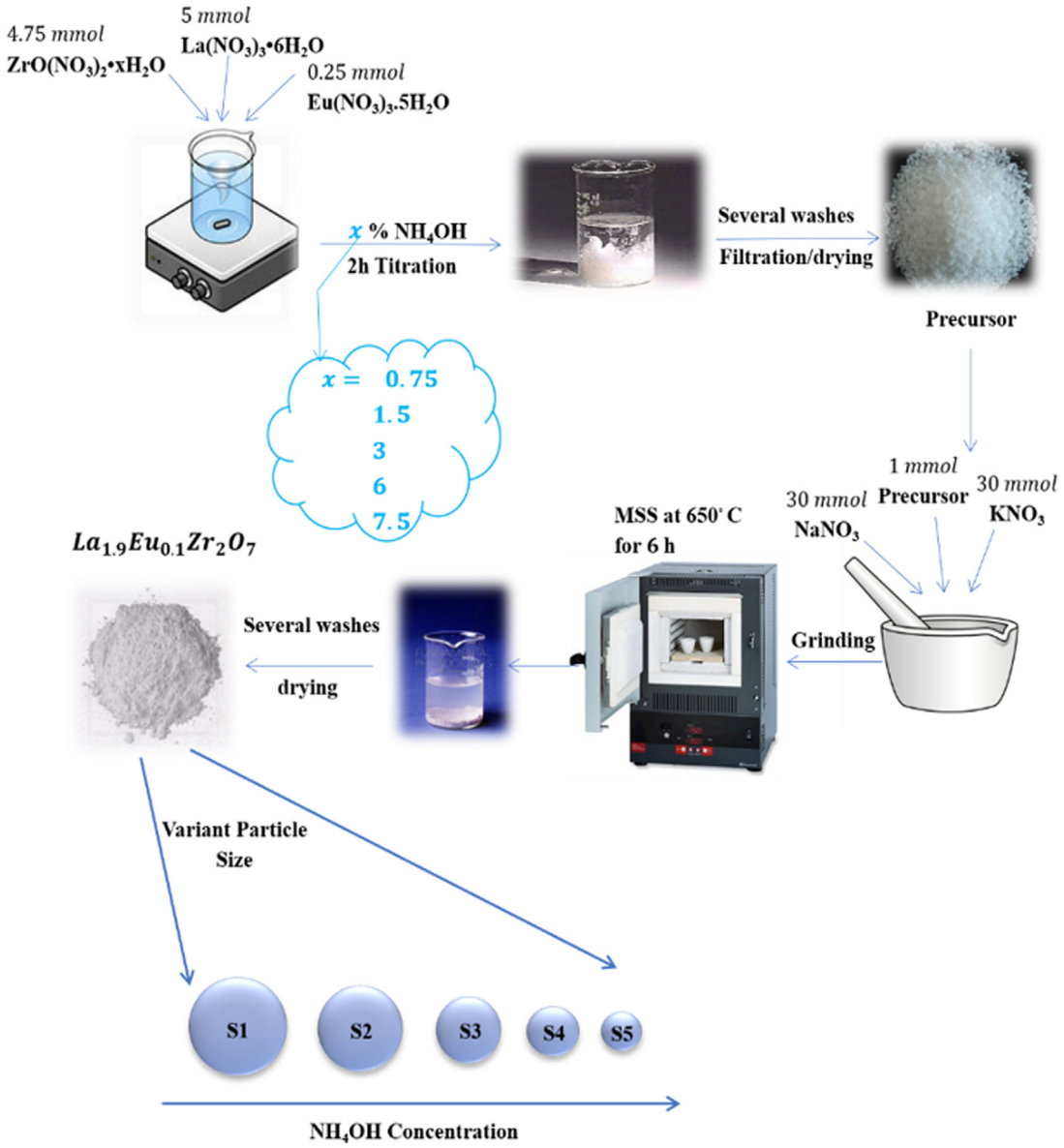

Fig. 1. Schematic of the MSS synthesis procedure for the undoped and 5%Eu^{3+}-doped $La_2Zr_2O_7$ NPs using different concentrations of precipitant NH_4OH solution. The schematic also reveals the size tunability of the obtained NPs by varying the concentration of NH_4OH.

luminescent materials. Moreover, it is expected that doping may shift the light emission of $La_2Zr_2O_7$ NPs. This may be due to host to dopant energy transfer, which can be feasible depending on the energy level diagram of host and dopant. It is very interesting to observe that in lanthanide doped inorganic compounds, host to dopant energy transfer is feasible for some cases and it is absent in some other cases [36–40]. Energy transfer plays an important role in the designing of tunable phosphors, so understanding the mechanism involved in the process gives a better insight into making highly efficient phosphors. In this context, we doped trivalent europium ions into LZO NPs for obvious reasons including the degenerated $^5D_0$ and $^7F_0$ states, the presence of pure magnetic dipole, the hypersensitive electric dipole transition, and the bright and narrow red band from the $^5D_0 \rightarrow {}^7F_2$ transition.

LZOE NPs were synthesized using a molten salt synthesis (MSS) method at 650 °C. MSS yields pure compounds at a relatively lower temperature compared to other high temperature ceramic routes. Moreover, using low melting molten salts, such as alkali halide, nitrate, nitrite, and sulphide, etc [41]., the rate of reaction is enhanced by increasing the contact area between reactants and the mobility of reactants within the molten salts. The obtained particles are highly monodisperse because Ostwald ripening governs the particle growth in molten salt.

In this study, we exploited another dimension of the MSS process to make different sized $La_2Zr_2O_7$:Eu^{3+} NPs by changing the coprecipitation pH using ammonium hydroxide (NH_4OH) solution. We then investigated its effect on various optical parameters of Eu^{3+} ions. Eu^{3+} ions being most extensively used as a spectroscopic probe are the right choice for this particular work. Eu^{3+} ions can easily sense any induced change in the optical properties due to the change of nanoparticle size. The difference from other studies is that the nanoparticle size variation is not created by heating temperature or annealing duration. Moreover, we exploited the effect of nanoparticle size on the radioluminescence properties of the LZOE NPs, which will help optimize it as an x-ray phosphor for medical applications. Therefore, this study focused on the low temperature MSS of the LZOE NPs and the effects of coprecipitation pH on their optical properties. Furthermore, density functional theory (DFT) based calculations were performed to identify the change in electronic density of states (DOS) due to oxygen vacancies (neutral and

charged). Origin of experimentally obtained emission in violet-blue and red optical regions is explained using DFT calculations.

2. Experimental

2.1. Synthesis of undoped and Eu-doped $La_2Zr_2O_7$ NPs

In this work, both undoped and 5% Eu^{3+} doped $La_2Zr_2O_7$ NPs were synthesized using a combined coprecipitation and MSS two-step procedure as reported in our earlier work [25,32]. To explore the effect of precipitating pH on nanoparticle size and optical properties of the LZO and LZOE NPs, we varied the concentration of NH_4OH in the coprecipitation step. The concentrations used were 0.75%, 1.5%, 3.0%, 6.0%, and 7.5% of commercial NH_4OH solution (aq., 28–30%). This coprecipitation step allowed for the formation of a complex single-source precursor $La(OH)_3{\cdot}ZrO(OH)_2{\cdot}nH_2O$ or $95\%La(OH)_3 0.5\%Eu(OH)_3{\cdot}ZrO(OH)_2{\cdot}nH_2O$ corresponding to the undoped or $5\%Eu^{3+}$ doped $La_2Hf_2O_7$ NPs. In the next MSS step, potassium nitrate (KNO_3, 99.9%), sodium nitrate ($NaNO_3$, 98%) and the formed single-source precursor were mixed in a weight ratio of 30:30:1 and grinded together into fine powder. Then the resulting mixture was transferred into a corundum crucible and placed in a muffle furnace. The furnace was set to run at 650 °C for 6 h with ramp-up and -down rates of 10 °C/min. The synthesized $La_2Zr_2O_7$ NPs and $La_2Zr_2O_7$:5%Eu^{3+} NPs were washed multiple times with deionized water to remove any residual salt from the surface of the NPs. Accordingly, the undoped samples are denoted as LZO-S0.75, LZO-S1.5, LZO-S3, LZO-S6, and LZO-S7.5, and the Eu^{3+} doped samples are represented as LZOE-S0.75, LZOE-S1.5, LZOE-S3, LZOE-S6, and LZOE-S7.5. The schematic of the synthesis process for these undoped and doped LZO NPs is presented in Fig. 1.

2.2. Instrumentation

The LZO and LZOE NPs were characterized using X-ray diffraction (XRD), Raman spectroscopy, scanning electron microscopy (SEM), photoluminescence (PL), radioluminescence (RL), fluorescence decay, quantum yield, and time resolve emission spectroscopy (TRES). To assess the crystal phase and purity of the synthesized NPs, XRD patterns were collected using BRUKER™ D8 Advance X-ray diffractometer with a Cu $K_{\alpha1}$ radiation (λ = 0.15406 nm, 40 kV, 40 mA) with a scanning mode in 2θ ranging from 10° to 90° and a scanning step size of 0.04° at a scanning rate of 2.0° min^{-1}.

The particle size was determined from the broadening of XRD reflections by using the Scherrer formula:

$$d = \frac{k\lambda}{B\cos\theta} \tag{1}$$

where d is the calculated crystallite size, λ is the wavelength of X-ray radiation, θ is the Bragg's angle, which is being fitted to calculate the full width half maxima (FWHM), B is the FWHM value in radians in 2θ scale, and k is a Scherrer constant.

To confirm the crystal structure of the synthesized NPs, Raman spectra were taken with a Renishaw Raman spectroscope with an InVia confocal Microscope using 532 nm laser having power of ~5 mW. The microstructure and morphology of the particles were studied using a Carl Zeiss sigma VP FESEM field emission scanning electron microscopy (SEM) equipped with a field emission gun operated at 5 kV and an energy dispersive spectroscopy (EDS) attachment. Brunauer, Emmett, and Teller (BET) surface area measurements were completed with a Gemini VII 3.04 Model 2390P serial# 775 Surface Area Analyzer with an evacuation rate of 300.0 mmHg m^{-1} in^{-1} at a saturation pressure of 768.764 mmHg and nitrogen as an analysis adsorptive. PL emission and excitation spectra were recorded using an Edinburgh Instrument FLS 980 fluorometer system having steady state xenon lamp source. On the other hand, lifetime was measured with a pulsed microsecond xenon lamp source having a frequency range of 1–100 Hz using time correlated single photon counting (TCSPC) technique. A 150 mm BenFlect coated integrating sphere was employed to measure absolute quantum yield. Using an integrating sphere, the quantitative excitation and emission spectra in the wavelength region of 550–750 nm from the LZOE NPs (under UV light excitation at 393 nm) were recorded. Spectral sensitivity of the spectrometer and sphere was modified using a calibrated lamp for spectral light throughput. Lastly, RL spectra were acquired with a silver X-ray source tube adapted to the Edinburgh Instruments FLS 980 fluorometer system at a power of 12 W (60 kV and 200 μA).

2.3. Theoretical calculation

2.3.1. Judd-Ofelt calculations

The chemical environment effect on the luminescent properties of Eu^{3+} ions can be better understood through Judd-Ofelt theory analysis of the transition intensity parameters of the LZOE NPs. For the present system, the index of refraction was calculated by standard Gladstone and Dale formula as suggested by Larsen and Burman [42]. Gladstone-Dale relation was used to calculate the refractive index of the $La_2Zr_2O_7$ nanoparticle:

$$\frac{n-1}{\rho} = k_1\frac{p_1}{100} + k_2\frac{p_2}{100} \tag{2}$$

where k_i = Gladstone-Dale coefficient of chemical species i, $(n-1)$ is refractivity, ρ is volumic mass, and p = percentage of chemical species i.

The determination of Ω_λ (λ = 2, 4, 6) parameters from emission spectra is necessary, where the magnetic dipole transition $^5D_0 \rightarrow {}^7F_1$ can be noted as follow:

$$A_{md} = \frac{64\pi^4}{3h(2J+1)}\nu_{md}^3 n^3 S_{md} \tag{3}$$

here, ν_{md} represents the energy of the magnetic dipole in wavenumber and h is Planck's constant, 6.626×10^{-34} J·s. In addition, the variable n depicts the refractive index of the host LZO as 1.99 and $2J' + 1$ is the degeneracy of the initial state (1 for $^5D_0$). Furthermore, S_{md} is a constant independent of the host and is equal to 9.6×10^{-42} [43]. The electric dipole transitions can be denoted by $^5D_0 \rightarrow {}^7F_J$ (J = 2, 4, and 6) transitions where the radiation rate can be stated as follows [44,45]:

$$A_J = \frac{64\pi^4}{3h}\frac{e^2\nu^3}{(2J+1)}\frac{n(n^2+2)^2}{9}\sum_{\lambda=2,4,6}\Omega_\lambda \langle \Psi J \| U^\lambda \| \Psi' J' \rangle^2 \tag{4}$$

In this equation, e is the electric charge, ν is the transition energy of electric dipole transitions in cm^{-1}, Ω_λ is the intensity parameter, and $\langle \Psi J \| U^\lambda \| \Psi' J' \rangle^2$ values are the squared reduced matrix elements, whose values are 0.0032 and 0.0023 for J' = 2 and 4, respectively [46]. In all the parameters of the equations, Gaussian units are used for ease of calculating. Therefore, the transition intensity ratio between electronic dipole and magnetic dipole can be written as follow:

$$\frac{\int I_J(\nu)d\nu}{\int I_{md}(\nu)d\nu} = \frac{A_J}{A_{md}} = \frac{e^2\nu_j^3}{\nu_{md}^3}\frac{(n^2+2)^2}{9n^2}\Omega_\lambda \langle \Psi J \| U^\lambda \| \Psi' J' \rangle^2 \tag{5}$$

which can be easily simplified as follow:

$$A_J = \frac{64\pi^4}{3h}\frac{e^2\nu^3}{(2J+1)}\frac{n(n^2+2)^2}{9}\Omega_\lambda \langle \Psi J \| U^\lambda \| \Psi' J' \rangle^2 \tag{6}$$

In Eq. (5), the value of $\frac{\int I_J(\nu)d\nu}{\int I_{md}(\nu)d\nu}$ can be acquired from the integral area of the emission spectra. In addition, Ω_λ can be determined from the calculated basis of the emission spectra. However, the Ω_6 intensity parameter is not included in this calculation due to the fact that $^5D_0 \rightarrow {}^7F_6$ transitions were not observed.

The internal quantum efficiency (IQE) of the $^5D_0$ level of Eu^{3+} ions in the LZOE NPs can be deduced using the emission spectra and lifetimes of the former electronic transition level. We can correlate the

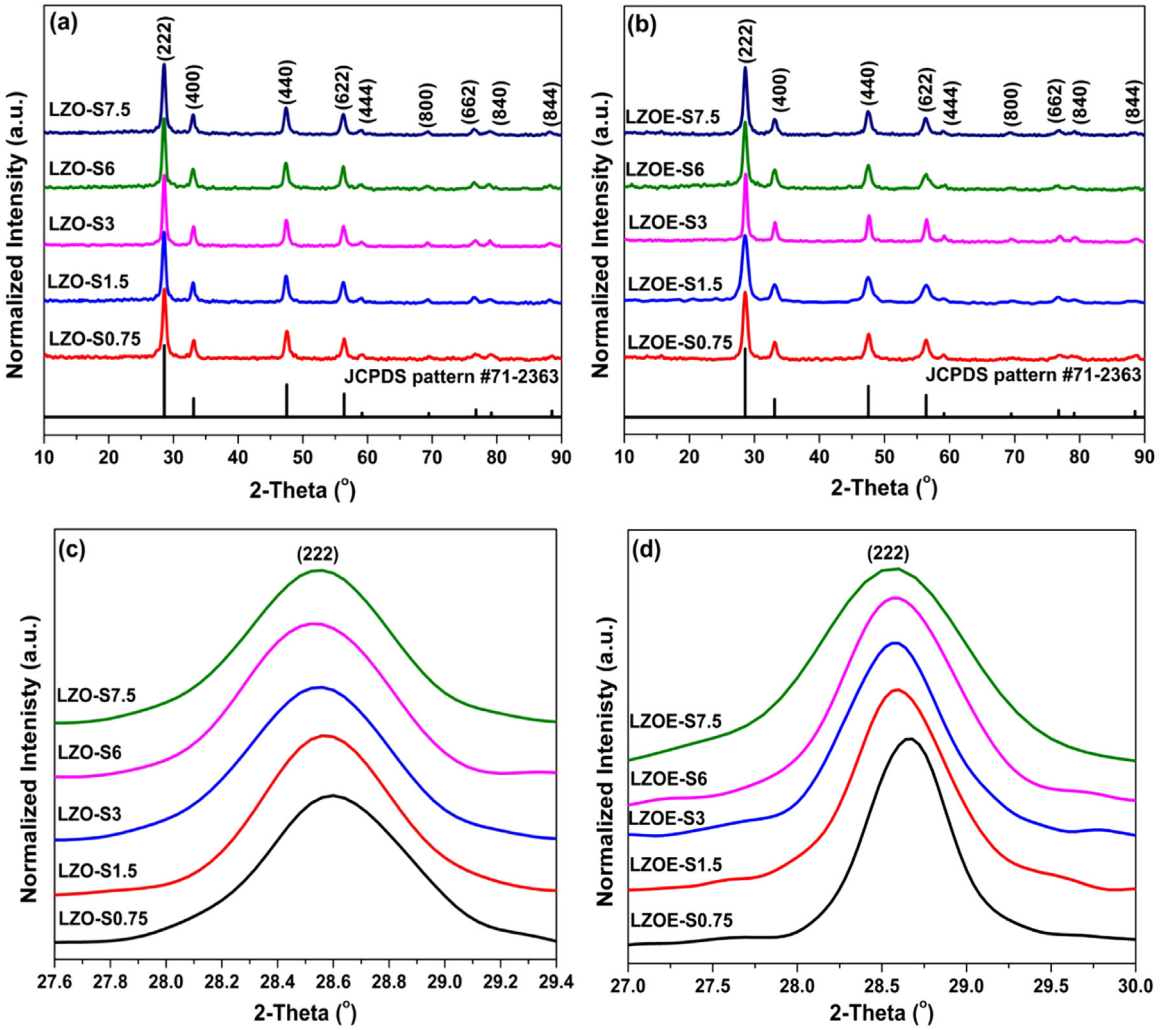

Fig. 2. XRD patterns of (a) LZO NPs and (b) LZOE NPs. Enlarged (222) diffraction peak of the (c) LZO NPs and (d) LZOE NPs.

lifetime (τ), radiative (A_R), and nonradiative (A_{NR}) rates through the following equation:

$$\frac{1}{\tau} = AR + ANR \tag{7}$$

here the AR rate can be determined by adding over the radiative rates for each $^5D_0 \rightarrow {}^7F_J$ (J = 1–4), $\sum_{J=1-4} A_J$. Therefore, the IQE of the emitting $^5D_0$ level is written as

$$IQE = \frac{A_R}{A_R + A_{NR}} = \tau \sum_{J=1-4} A_J \tag{8}$$

In this case, the radiative contribution can be calculated from the relative intensities of the $^5D_0 \rightarrow {}^7F_J$ (J = 1–4) transitions. The $^5D_0 \rightarrow {}^7F_{5,6}$ branching ratios $\left(\beta_J = \frac{A_J}{\sum A_J}\right)$ are neglected since both have poor relative intensity compare to the $^5D_0 \rightarrow {}^7F_{1-4}$ transitions.

2.3.2. Density functional Theory Calculations

To determine the charge transfer level with the Eu^{3+} doping in LZO, the oxygen defect formation energies of 0, +1 and +2 charge are now calculated with Eu^{3+} doping in La/Zr site. For this purpose, GGA + U methodology is adopted to model f-f interaction of Eu^{3+} atom. The Hubbard U correction was introduced using the method proposed by Dudarev et al. [47] in which the U parameter (which reflects the strength of on-site Coulomb interactions) and the J parameter (which adjusts the strength of exchange interactions) are combined into a single parameter U_{eff} = U - J to account for the Coulomb repulsions between localized f-electrons. The value that we employed was U_{eff} (Eu) = 10.9 eV, as proposed by Richard et al. [48]

All the electronic structure calculations of ideal, oxygen defects structures and Eu^{3+} doping in LZO were performed using a plane wave based spin-polarized density functional theory (DFT) as implemented in Vienna Ab-intio Simulation package (VASP)[49,50]. The electron-ion interaction was described by projector augmented wave (PAW) potential [51] which includes the valence states of La ($5s^2 5p^6 5d^1 6s^2$ – 11 valence electrons), Zr ($4s^2 4p^6 5s^2 4d^2$ – 12 valence electrons), O ($2s^2 2p^4$ – 6 valence electrons) and Eu ($5s^2$ $5p^6$ $4f^7$ $6s^2$ – 17 valence electrons). For the exchange-correlation potential, local gradient approximation (LDA) and generalized gradient approximation (GGA) with Ceperley–Alder parameterization and Perdew-Burke-Ernzerhof (PBE) parameterization [52], respectively, were used. A Monkhorst-Pack [53] k-space mesh of 12 × 12 × 12 and 6 × 6 × 6 in reciprocal space for the Brillouin zone integration was used for 22 atoms and 88 atoms cells, respectively. The plane wave cutoff energy (E_{cut}) of 500 eV for basis set was used throughout the simulation. The optimization was carried out to get converged values for E_{cut} and k-point meshes which ensure convergence of total energy to within a precision of 0.05 meV/atom for cubic ideal and defective pyrochlore unit-cell/supercell. The cohesive energy of LZO was optimized with respect to volume (or lattice parameter) and atomic positions using conjugate gradient algorithm until the residual forces and stress in the equilibrium geometry were of the order of 0.005 eV/Å and 0.01 GPa, respectively. The final calculations of total electronic energy and density of states (DOS) were performed

using the tetrahedron method with Blöchl corrections [54].

In order to calculate DOS and defect formation energies of LZO with oxygen defects and Eu doping, 88 atom supercell (2 ×2 ×2 supercell of 22 atoms ideal pyrochlore) was used. To study the effect of Eu doping, one Eu atom was replaced in place of La/Zr atom in 88 atom supercell. In addition, to generate defect structure an oxygen atom was removed from an 88 atom supercell and defect structures were thoroughly optimized with respect to atomic positions as described in previous paragraph. Therefore, defect concentration in our calculation was 1/88 or 1.136%.

We further applied the screened hybrid functional of Heyd, Scuseria, and Ernzerhof (HSE06) functional [55] to take into account the effects of nonlocal exchange. In these calculations, the screened exchange functional with 25% Hartree-Fock contribution and a screening length of 0.2/Å were used. For the HSE06 calculations a Γ-centered 2 × 2 × 2 k-point grids for the sampling of Brillouin zone (BZ) of 88 atom supercells were used considering computational burden of the HSE06 calculations. The HSE06 calculations were performed using charge density generated from the GGA calculations to get accurate band-gap energies for the ideal LZO.

3. Results and discussion

3.1. Materials characterization

3.1.1. Powder X-ray diffraction

To synthesize LZO NPs with different sizes we have varied the pH value of the coprecipitation solution by changing the NH_4OH concentration. The phase purity of the LZO and LZOE samples were confirmed using powder XRD as shown in Fig. 2a and b, respectively. The standard JCPDS card (No. 71-2363) of $La_2Zr_2O_7$ was also presented for comparison. It could be observed that all diffraction peaks well match with the JCPDS file 71-2363 indicating the formation of pure LZO and LZOE with high crystallinity.

The only change observed from the XRD data is the difference of crystallite size (Table 1). There is a progressive decrease of crystallite size as the coprecipitation pH is raised. This can be observed in Fig. 2c and d wherein the (222) peak becomes broader with increasing the pH value of the coprecipitation solution, which indicates the decrease of crystallite size. The decrease in the crystallite size has been attributed to the fact that higher concentration of the added NH_4OH solution enables more nuclei for the single-source precursor, so the size of the amorphous single-source precursor particles decreases, which eventually gives smaller final LZO and LZOE NPs [56]. The reduction in crystallite size with the increase of precipitation pH has also been observed in zinc oxide and lutetium oxide NPs [57,58].

In addition, the Eu^{3+} ions are expected to replace the La^{3+} ions due to the same valence states and similar radius values ($R_{La^{3+},CN=8}$ = 1.16 Å, $R_{Eu^{3+},CN=8}$ = 1.07 Å). These XRD results confirmed that the Eu^{3+} ions enter substitutionally in the $La_2Zr_2O_7$ host lattice, and do not change the basic $La_2Zr_2O_7$ structural network, and the replacing of La^{3+} by Eu^{3+} ions did not lead to a phase change.

Table 1
Crystallite size calculated by the Debye-Scherrer equation of the LZO and LZOE NPs.

NH_4OH(aq) Concentration	pH	Crystallite size (nm)	
		LZO	LZOE
0.75%	11.7	22.70 + /- 0.751	24.70 + /- 0.630
1.5%	12.1	20.91 + /- 0.781	22.87 + /- 0.655
3.0%	12.2	18.48 + /- 0.832	19.58 + /- 0.708
6.0%	12.4	16.55 + /- 0.879	18.57 + /- 0.727
7.5%	12.5	12.41 + /- 1.015	15.88 + /- 0.786

3.1.2. Raman spectroscopy

There are two common phases of the $A_2B_2O_7$ compounds, i.e. disordered fluorite and ordered pyrochlore phases. The disordered fluorite phase exists in $Fm\bar{3}m$ space group wherein all the cationic ions (A^{3+} and B^{4+}) are randomly distributed allowing for one active mode. On the other hand, ordered pyrochlore phase exist in $Fd\bar{3}m$ space group. Therefore, it exhibits close structural resemblance to fluorite phase except that there are two cationic sites, three anionic sites 48f(O_I), 8a (O_{II}), and 8b(O_{III}), and 1/8th of the oxygen ions (O_{III}) at 8b site absent in the pyrochlore structure allowing for 6 active modes [59–61]. Based on the group theory, the defect fluorite structure has one vibrational mode due to T_{2g}, while a pyrochlore phase has six vibrational modes in the range of 200–1000 cm^{-1}. This information is vital for the correct phase identification of the LZO and LZOE NPs. Raman spectra indicate that they have a typical ideal pyrochlore structure with characteristics 6 vibrational modes [5,25,62] (Fig. 3a and b). The insets in these figures represent the LZO and LZOE NPs prepared with the highest NH_4OH concentration. All the peaks corresponding to pyrochlore phase were fitted with a Gaussian function to express their location and number of peaks. In addition, there is no change after Eu^{3+} doping, nor obvious change as a function of the coprecipitation pH. However, the Raman peaks narrow down with increasing coprecipitation pH, which indicates an increase of structural ordering, and the LZOE-S7.5 NPs have the most ordered structure among all of the samples.

3.1.3. Scanning electron microscopy

To investigate the effect of precipitating pH on the microstructure of the LZOE NPs, SEM measurements were carried out (Fig. 4a–e). It can be seen that the LZOE NPs have regular shape and uniform size distribution. The size of individual particles is about 10–40 nm, and the shape and size of the NPs are nearly unchanged as a function of the used precipitation pH. The SEM images display certain degree of soft agglomeration, which formed during the SEM sample drying process. Particle size distribution histograms were obtained using the ImageJ software. The size of these nanoparticles decreases with the increasing precipitation pH value. This is in agreement with the calculated crystallite size from our XRD data using the Debye-Scherrer equation. The importance of synthesizing nanoparticles comes from many benefits available from them when compared to their bulk counterparts, which include superior mechanical strength, thermal stability, catalytic activity, electrical conductivity, magnetic properties, and optical properties. In addition, nanophosphors can be easily used for bioimaging, drug delivery, making composite with film and fibers for optoelectronics, and superior scintillation efficiency, etc.

To confirm Eu^{3+} doping into the LZO NPs, EDS spectra on the LZOE NPs (Fig. 4f) have been carried out. The distinct X-ray absorption edge binding energies of La, Zr, O and Eu in the EDS spectra confirm the high purity of the synthesized NPs. The EDS analysis clearly indicated the presence of europium ion in the $La_2Zr_2O_7$ NPs. The C and Al peaks arise from the use of carbon tape and aluminum sample holder.

3.1.4. Surface area measurement

Nanoparticles are very rich in surface defects that have profound influence on their performance as phosphors as well as scintillators. To see the changes in defect density as a function of pH we have carried out Brunauer, Emmett, and Teller (BET) surface area measurement. BET N_2 adsorption isothermal measurements were performed to measure the specific surface area of the LZOE NPs (Fig. 5a). The BET adsorption relation is given by Eq. (9) below:

$$\frac{1}{Q\left[\left(\frac{P_0}{P}\right)-1\right]} = \frac{C-1}{Q_m C}\left(\frac{P}{P_0}\right) + \frac{1}{Q_m C} \quad (9)$$

where P and P_0 are the equilibrium and saturation pressures, respectively, Q is the amount of the nitrogen gas adsorbed on the adsorbate, Q_m is the monolayer adsorbed gas quantity, and C is the BET constant. A

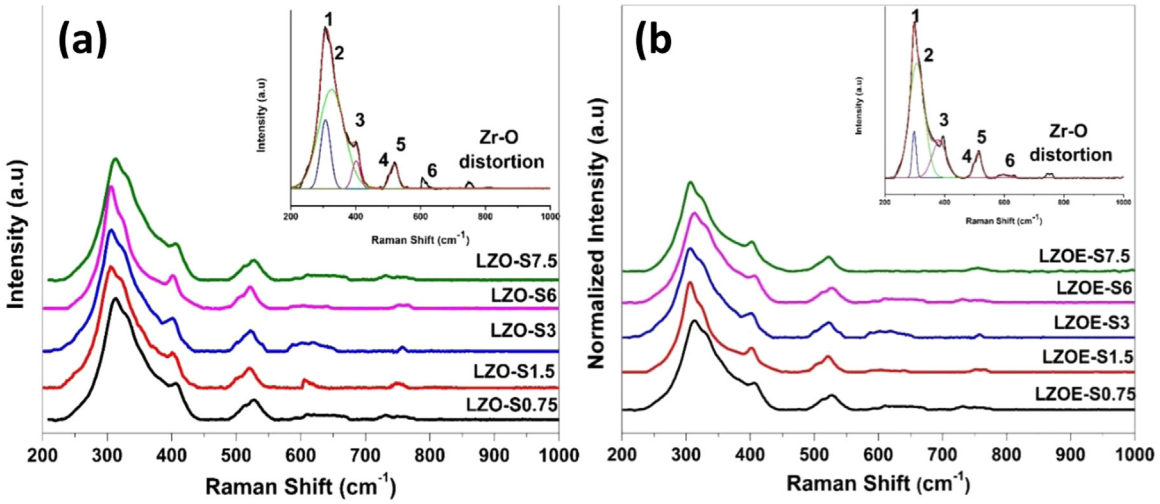

Fig. 3. Raman spectra of (a) the LZO and (b) LZOE NPs.

BET adsorption isotherm plots of $\frac{1}{Q[\left(\frac{P_0}{P}\right)-1]}$ vs. $\left(\frac{P}{P_0}\right)$ based on Eq. (9) (Fig. 5b) give the calculated BET surface area values (Table 2). From this table, BET surface area increases progressively as the used precipitation pH value increased from 11.7 to 12.5 or on going from samples S0.75 to S7.5. This is in a good agreement with the XRD and SEM data discussed earlier.

3.2. DFT study on LZO NPs

3.2.1. Correlating observed photoluminescence of $La_2Zr_2O_7$ with DFT calculations

Table 3 shows our DFT calculated equilibrium lattice parameters, internal parameters, bond lengths and electronic band-gaps using LDA and GGA approximations compared with those from previous experiments and first-principles calculation. Compared to the experimental data, our GGA and LDA calculated values are overestimated and underestimated, respectively. However, our calculated lattice parameters match with the experimental values within 1.5% difference, and the GGA approximation gives the closest value relative to the experimental data. Both LDA and GGA calculated internal parameters and bond-lengths match within 5% variation to the experimental values.

The LZO NPs displayed a very broad excitation band at around 306 nm and a small peak at 380 nm (Fig. 6a). The intense excitation band at 306 nm is attributed to intrinsic electronic transition within the ZrO_6 polyhedra. The small peak around 380 nm may be due to some structural defects, e.g. cation/anion vacancies or ZrO_6 distortion. The emission spectrum (Fig. 6b) under 306 nm excitation displayed a dual band feature with violet-blue and red emissions around 400 and 700 nm, respectively. Considering the large band gap of $La_2Zr_2O_7$, the emission around 400 nm (violet-blue) is not due to exciton emission. However, it is in close resemblance with the oxygen vacancy related emission in ZrO_2, which is attributed to the $^2T_{1u} \rightarrow {}^2A_{1g}$ transitions of F^+ center around the octahedral Zr atom [65]. The red emission band around 707 nm band can be assign to the transition of electron trapped at the shallow states to the vacant deep states due to singly charged

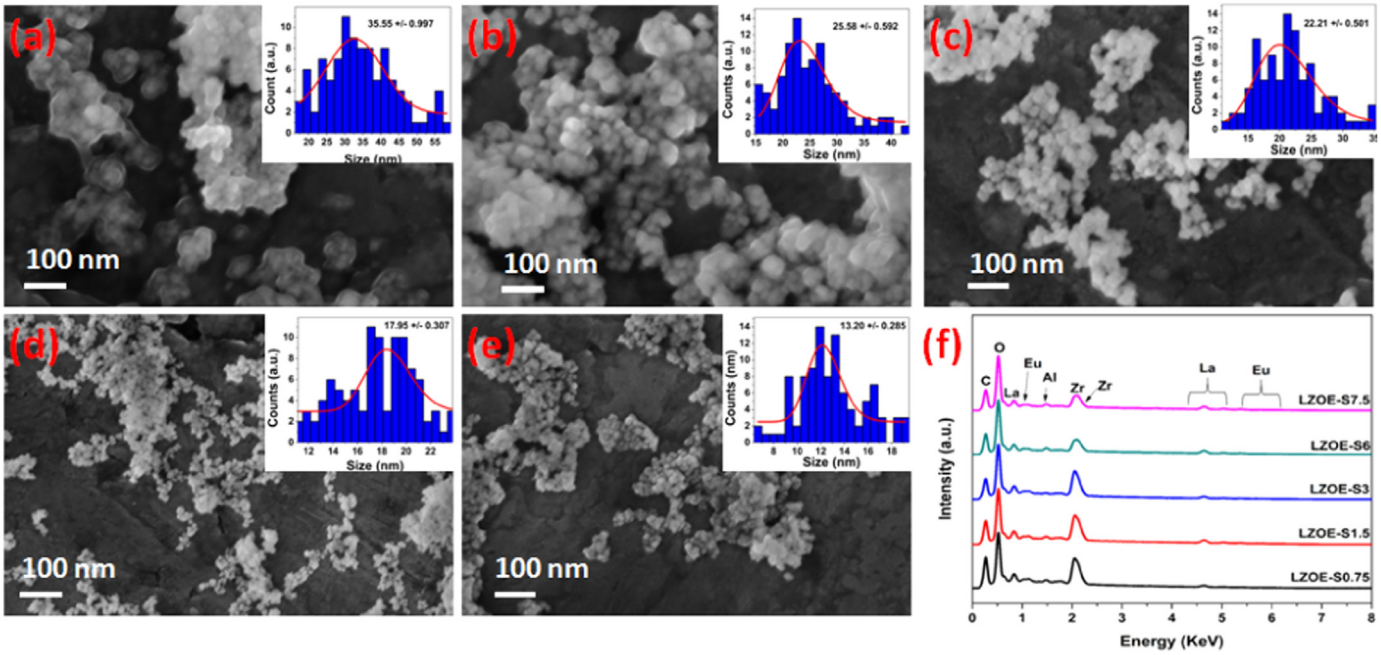

Fig. 4. SEM images of the LZOE NPs prepared from the precursors precipitated at different NH_4OH concentrations: (a) LZOE-S0.75, (b) LZOE-S1.5, (c) LZOE-S3, (d) LZOE-S6, and (e) LZOE-S7.5. (f) EDS spectra of the LZOE NPs.

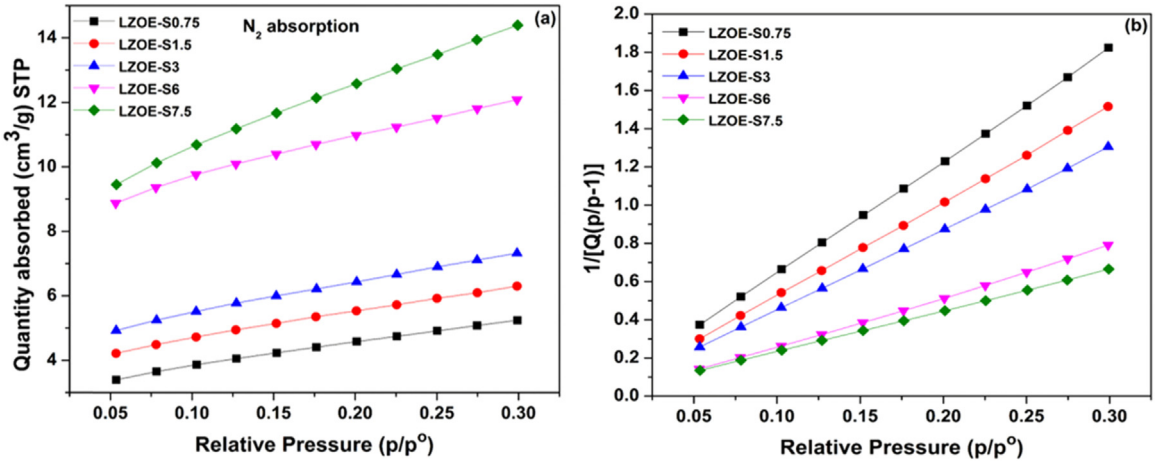

Fig. 5. (a) N_2 adsorption isotherm and (b) the fitting curve of the BET surface area of the LZOE NPs.

Table 2
BET surface area and QY of the LZOE NPs.

Samples	BET surface area (m^2/g)
LZOE-S0.75	16.4990 + /- 0.0606
LZOE-S1.5	19.6825 + /- 0.0897
LZOE-S3	22.8693 + /- 0.1023
LZOE-S6	37.2061 + /- 0.4108
LZOE-S7.5	45.0669 + /- 0.1656

paramagnetic V_O^{+}. Previously oxygen vacancy induced emissions in blue and green regions have been observed from $Gd_2Zr_2O_7$ and $Nd_2Zr_2O_7$ [1,66]. PL decay curve clearly shows oxygen defect mediated PL emission properties in the samples. Based on the relationships of the emission and excitation intensities with the coprecipitation pH, the LZO-S0.75 sample displayed the best performance. This can be attributed to the least surface defects due to the large size of the LZO-S0.75 NPs.

Fig. 7 shows the emission profiles of the $La_2Zr_2O_7$ NPs annealed in oxygen and hydrogen atmosphere and compared to that of the as-synthesized LZO- NPs. It is interesting to observe that the intensity of blue/red emission decreases after annealed in oxygen atmosphere while it enhances after annealed in argon/H_2 atmosphere compare to that of the original NPs synthesized in air. O_2 molecules presented in oxygen environment could combine with oxygen vacancies presented in the original LZO NPs during the annealing process, so the emission intensity decreases. On the other hand, in the presence of the reducing atmosphere of argon/H_2, more oxygen vacancies are involved compare to the as-synthesized NPs, therefore the emission intensity of the LZO NPs is enhanced.

3.2.2. Defect formation energies

The defect formation energy is given by

$$E_f^q = E_{defect}^q - E_{perfect} - \sum_\alpha n_\alpha \mu_\alpha + q_i \mu_e + dE \quad (10)$$

where E^q_{defect} and E_{perfect} are the DFT(GGA) total energies of the system with and without the defect, respectively, n_α is the number of atoms added/removed, μ_α is the chemical potential of the species α that is added/removed, q_i is the effective charge on the defect and

$$\mu_e = E_{VBM} + \varepsilon_F. \quad (11)$$

E_{VBM} is the energy of the valence band maximum (VBM) and ε_F is the electron chemical potential above the VBM. dE is a correction used to mitigate the interactions of the defect charges with their periodic images. Here we employ a Madelung correction as proposed by Leslie and Gillan [67] employing the experimental dielectric constant of 22.8 [68].

To see how the defect formation energies of oxygen vacancies in the dilute limit varies as a function of Fermi energy, we summarized DFT calculated formation energies in Fig. 8 (left panel). The calculated vacancy formation energy values indicate that the formation of V_O^{+2} defects is favored in the 0–1.4 eV (in E_F-E_V scale) near the valence band compared to V_O^{+1} and V_O° oxygen defects, indicating that oxygen vacancies tend to donate electrons or behave as a n-type defect. Similarly, the formation of V_O^{+1} defect is favored in the 1.4–5.2 eV (in E_F-E_V scale) and afterwards formation of V_O° is favorable. The DFT-GGA and HSE06 calculated electronic band-gap of LZO is 3.68 eV and ~5 eV, respectively. We are unable to compare band-gap values as no experimental band-gap is reported in the literature.

Fig. 8 (right panel) shows that the defect exhibits two charge-state transition levels: one deep donor level $\varepsilon(+2/+1)$ at 1.4 eV and another deep donor level $\varepsilon(+1/0)$ at 5.2 eV (left panel). In this case, the impurity levels are defined as the charge-state transition levels ($\varepsilon(q_1/q_2)$, from q_1 to q_2), i.e. the Fermi level locations at which two charge states of the defect have the same formation energy. The obtained impurity levels are shown in a conventional band diagram with respect to the host referred binding energies (HRBE). The charge-state transition level

Table 3
GGA and LDA calculated equilibrium lattice parameters, atomic positions, bond-lengths and band-gap along with previous experimental measurements and HSE06 calculated electronic band-gap.

$La_2Zr_2O_7$	a_0 (Å)	x	La-O_{8b} (Å)	La-O_{48f} (Å)	Zr-O_{48f} (Å)	Band-gap (eV)
GGA	10.888	0.333	2.36	2.65	2.13	3.68
LDA	10.692	0.335	2.31	2.59	2.10	3.51
HSE06	–	–	–	–	–	4.93
Experimental	10.805 [62]	0.332 [62]	2.339 [62]	2.635 [62]	2.105 [62]	–
	10.800 [63]	0.333 [63]	2.340 [63]	2.640 [63]	2.100 [63]	
DFT-LDA	10.720 [64]	0.331 [64]	2.320 [64]	2.620 [64]	2.090 [64]	

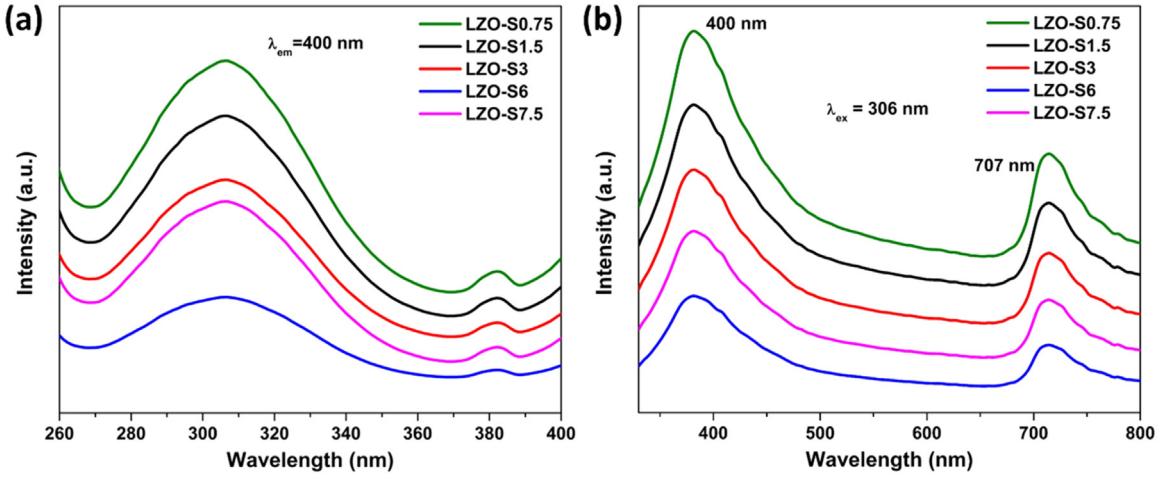

Fig. 6. (a) Excitation and (b) emission spectra of the LZO NPs.

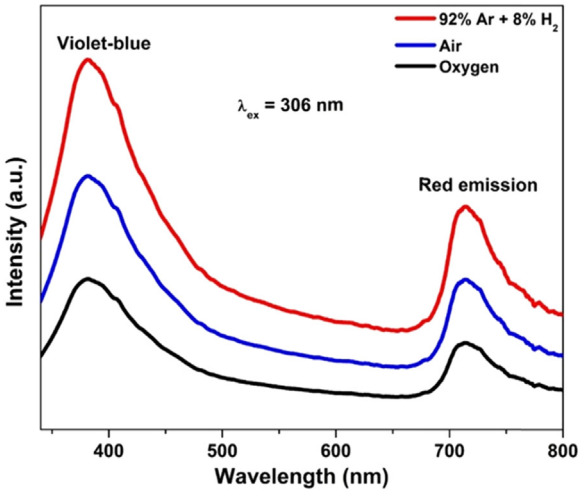

Fig. 7. Emission spectra of the LZO NPs (LZO-S0.75) annealed in reducing and oxidizing atmospheres and comparison with that from the original LZO NPs.

situated at 1.4 eV and ~5 eV can be attributed to the defect related emission at 700 and 400 nm.

3.3. PL spectra of the LZOE NPs

3.3.1. Excitation and emission properties

Fig. 9a shows the excitation spectra of the LZOE NPs monitored at 612 nm, which corresponds to the $^5D_0 \rightarrow {}^7F_2$ transition. The spectra consist of a broad band in the region of 240–300 nm and several narrow peaks in the range of 350–500 nm. The broad band is known as charge transfer state (CTS) and has combined contribution from various electronic transitions of O→Eu, O→Hf and Hf→Eu while the dominant one is the O→Eu transition. The excitation peaks around 361, 378, 393, 412 and 465 nm are attributed to intra f-f transitions of Eu^{3+} ions due to $^7F_0 \rightarrow {}^5D_4$, $^7F_0 \rightarrow {}^5L_{7,8}$; $^7F_0 \rightarrow {}^5L_6$, $^7F_0 \rightarrow {}^5D_3$ and $^7F_0 \rightarrow {}^5D_2$, respectively. The PL excitation intensity gradually decreases with the precipitation pH employed increases.

The LZOE NPs show very bright red luminescence when excited at 276 nm with a UV lamp (Fig. 9b) with similar spectral profiles, which are attributed to Eu^{3+} transitions from the excited $^5D_0$ state to ^7F_J (J = 0, 1, 2, 3 and 4) states. The dominant peaks are located at 579, 592, 613, 654, and 710 nm, corresponding to $^5D_0 \rightarrow {}^7F_0$, $^5D_0 \rightarrow {}^7F_1$, $^5D_0 \rightarrow {}^7F_2$, $^5D_0 \rightarrow {}^7F_3$, and $^5D_0 \rightarrow {}^7F_4$ transitions of Eu^{3+} ions, respectively. The intensity of $^5D_0 \rightarrow {}^7F_0$ transition is the weakest one because it is forbidden by electric dipole transition (EDT) and magnetic dipole transition (MDT). The most intense transition ($^5D_0 \rightarrow {}^7F_2$) is at 612 nm as the hypersensitive EDT. It is strongly affected by external factors like crystal

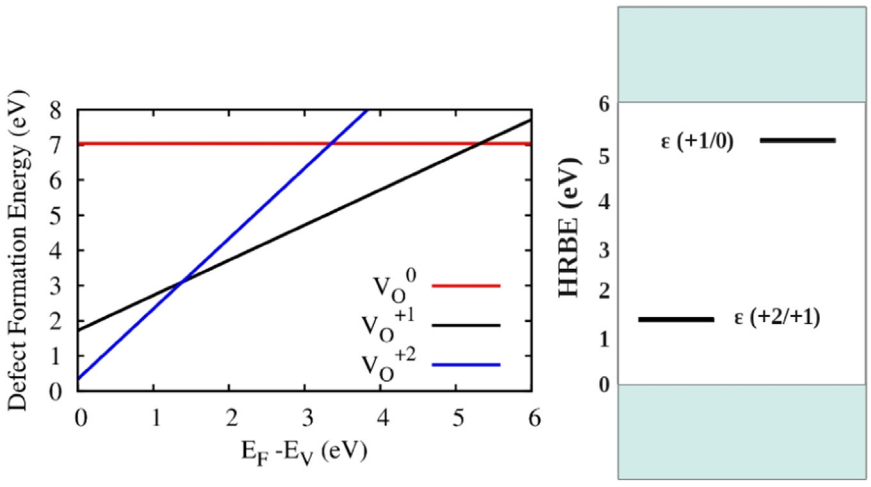

Fig. 8. GGA calculated defect formation energy (E_f) versus Fermi level (E_F) for three charge states q = 0, + 1 and + 2. The defect exhibits two charge-state transition levels: a deep donor level $\varepsilon(+2/+1)$ at 1.4 eV and another deep donor level $\varepsilon(+1/0)$ at 5.2 eV (left panel). The obtained impurity levels are shown in a conventional band diagram with respect to the host referred binding energies (HRBE) (right panel).

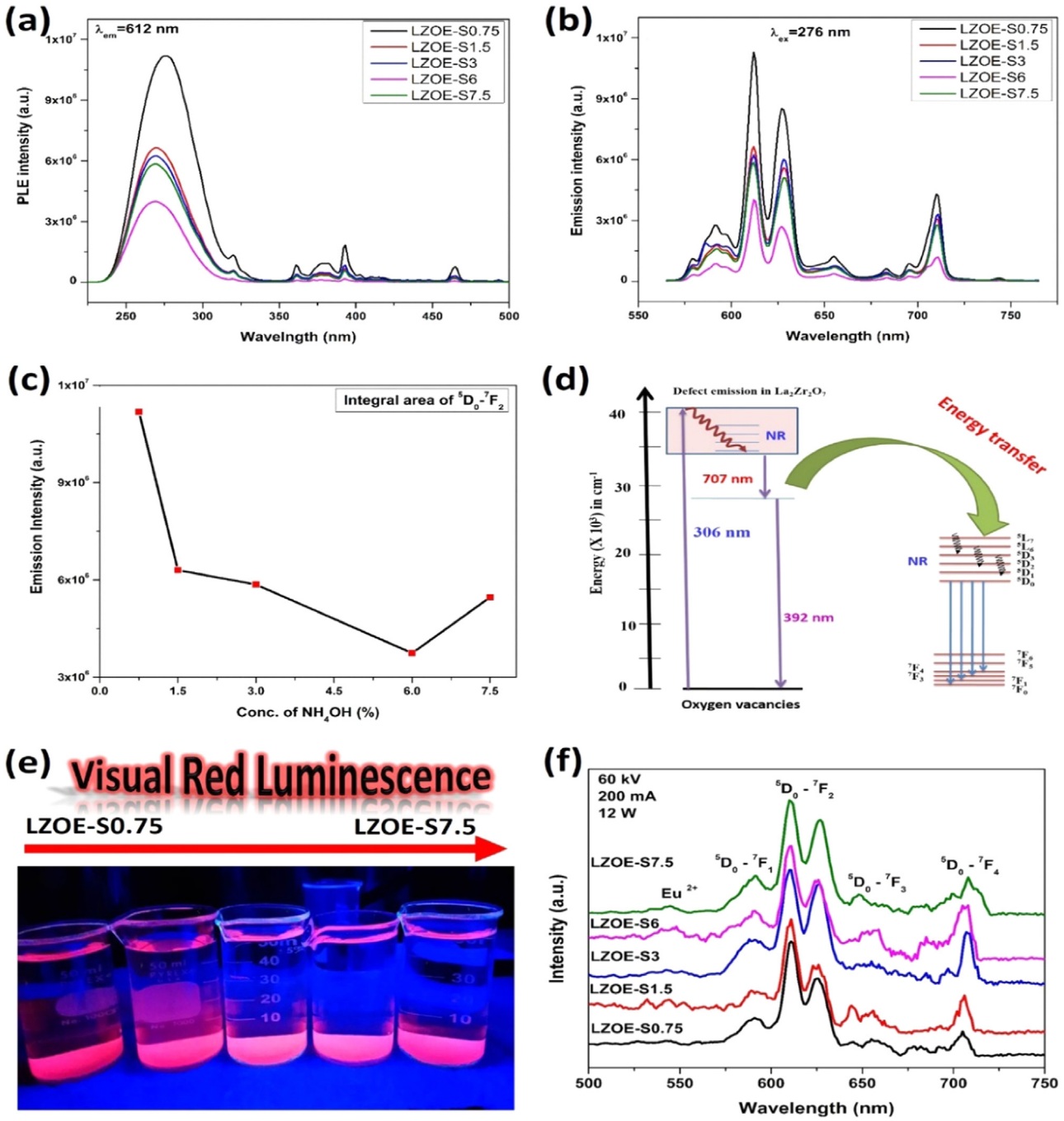

Fig. 9. (a) Excitation and (b) emission spectra of the LZOE NPs, (c) the relationship of PL emission intensity and the coprecipitation pH. (d) Proposed mechanism for energy transfer upon excitation from the LZO host to Eu^{3+} ions. (e) Digital images of the red LZOE NP phosphors under the excitation of a 393 nm lamp in the daylight. (f) RL spectra of the LZOE NPs.

Table 4
Asymmetry ratio and QY of the LZOE NPs.

Samples	Asymmetry ratio	Quantum yield (%)
LZOE-S0.75	4.05	10.34
LZOE-S1.5	3.67	10.01
LZOE-S3	3.46	9.88
LZOE-S6	4.67	8.62
LZOE-S7.5	3.68	9.74

field, local symmetry, dopant concentration, and thermal effects, etc. On the other hand, the intensity of the $^5D_0 \rightarrow {}^7F_1$ MDT is considerably low. This suggested that Eu^{3+} ions are localized in non-centrosymmetric sites in $La_2Zr_2O_7$ host, which is in close agreement with the crystal structure data (Fig. 3). This is further confirmed by high asymmetry ratio $(^5D_0 \rightarrow {}^7F_2)/(^5D_0 \rightarrow {}^7F_1)$ of 3.4–4.7 (Table 4) as an indication of high level of structural distortion from the inversion symmetry around the local environment of Eu^{3+} ions in the LZO lattice. From our Raman spectroscopic analysis, we have found that LZOE stabilizes in ideal pyrochlore structure (IPS). In IPS, a cation exists in highly distorted 8-fold coordinated scalenohedra whereas B-ion exist in highly symmetric octahedral in 6-fold coordination. In the LZOE NPs,

LaO_8 is highly distorted scalenohedra whereas ZrO_6 is an ideal octahedra with high level of symmetry. Eu^{3+} dopants are more likely to substitute La^{3+} due to closeness in ionic radius and the same ionic charge.

The PL emission intensity progressively decreases as the precipitation pH for the complex single-source precursor increases up to the LZOE-S6 NPs (Fig. 9c). The initial PL intensity decrease is correlated with the increasing number of surface defects (Table 2) as the source of non-radiative pathways. For commercial application of phosphors, their quantum yields are one of the most important parameters that need to be determined. The quantum yield of the LZOE NPs (Table 4) follows the same trend with the emission output for the same reason. The LZO NPs display multicolor emissions due to the presence of oxygen vacancies (Fig. 5). However, these oxygen vacancy-based emissions are absent, indicating complete photon energy transfer to Eu^{3+} ions in the LZOE NPs. Such host sensitized energy transfer is very important in realizing tunable phosphors. Accordingly, we have proposed the LZO host to Eu^{3+} energy transfer mechanism (Fig. 9d). To visualize the Eu^{3+} luminescent reduction on increasing the pH, digital images of the as-prepared red phosphors under the NUV light excitation at 393 nm have been shown in Fig. 9e. Evidently, the decrease of luminescence intensity from Eu^{3+} in LZOE NPs as the concentration of NH_4OH was increased from LZOE-S0.75 to LZOE-S7.5. To wash off the molten salt used in the synthesis from the surface of the formed nanoparticles, the as-synthesized samples were placed in distilled water and washed several times. The nanoparticle samples as stable metal oxides are not soluble in water. The digital photos (Fig. 9e) were taken while the nanoparticles were in the washing stage.

3.3.2. RL

The RL emission spectra of the LZOE NPs under X-ray excitation (Fig. 9f) is quite similar to their PL emission spectra (Fig. 9b) with typical emission lines of Eu^{3+} 4*f*–4*f* transitions in the red spectral region. No host-related emission in violet-blue spectral region was observed. The highest emission intensity was obtained from the LZOE-S0.75 NPs owing to the lowest surface defect density. It is worth noting that the absolute emission intensity of phosphors in powder form is rather sensitive to experimental arrangement, so the measured RL intensity cannot be the sole indicator of quenching. Unlike PL, the RL intensities of $^5D_0$–$^7F_3$ and $^5D_0$–$^7F_4$ transitions are even weaker. Similar to PL, the most intense RL transitions are $^5D_0 \rightarrow {}^7F_1$ MDT and $^5D_0 \rightarrow {}^7F_2$ EDT.

Table 5
Luminescence lifetime values of the LZOE NPs.

Sample	λ_{ex} = 276 nm		Average lifetime
	τ_s (ms)	τ_L (ms)	
LZOE-S0.75	0.88	2.30	1.61
LZOE-S1.5	0.96	2.34	1.81
LZOE-S3	1.00	2.60	2.07
LZOE-S6	0.75	2.14	1.46
LZOE-S7.5	1.00	2.47	2.01

3.3.3. PL lifetime

Fig. 10a shows the luminescence decay curves of the LZOE NPs when excited at 393 nm and emission monitored at 613 nm. The decay curves show a biexponential behavior with a noticeable double slope fitting. This suggests that there are two kinds of local environments of Eu^{3+} ions with two depopulation mechanisms from $^5D_0$ level. This phenomenon could be attributed to the stabilization of Eu^{3+} ions at highly asymmetric LaO_8 site and at perfectly ordered ZrO_6 site. The Eu^{3+}@La^{3+} and Eu^{3+}@Zr^{4+} doping decay at different rates although the fraction of the Eu^{3+}@La^{3+} doping is more than that of the Eu^{3+}@Zr^{4+} doping. The individual and average lifetime values of the LZOE NPs are presented in Table 5. The long lifetime is attributed to Eu^{3+}@Zr^{4+} with symmetric environment and forbidden f-f transitions. On the other hand, the short lifetime is attributed to Eu^{3+}@La^{3+} with asymmetric environment and allowed f-f transitions. Europium ions exhibit biexponential decays in other pyrochlores such as $La_2Hf_2O_7$, $Gd_2Zr_2O_7$, and $Nd_2Zr_2O_7$ wherein one of the lifetimes is attributed to rare earth A site occupancy and other to Hf/Zr site [2,3,69–73]. Normally the short lifetime is attributed to asymmetric environment as f-f transition becomes relaxed and the long lifetime is mostly attributed to symmetric environment as f-f transition is La-Porte forbidden [71,74–77]. The variation trend of the lifetime values as a function of the precipitating NH_4OH concentration (Fig. 10b) is slightly different from that of emission intensity (Fig. 9c). It initially increases, then decreases, and then increases again with the increasing precipitating NH_4OH concentration. As shown in Table 2, the BET surface area monotonically increases as the precipitation pH increases, which is attributed to the reduction in particle size of the LZOE NPs as a function of the precipitation pH. Surface area of NPs drastically influences the PL intensity that is present in the case of NPs [1] because the abundant surface defects, which is directly proportional to the surface area, provide non-

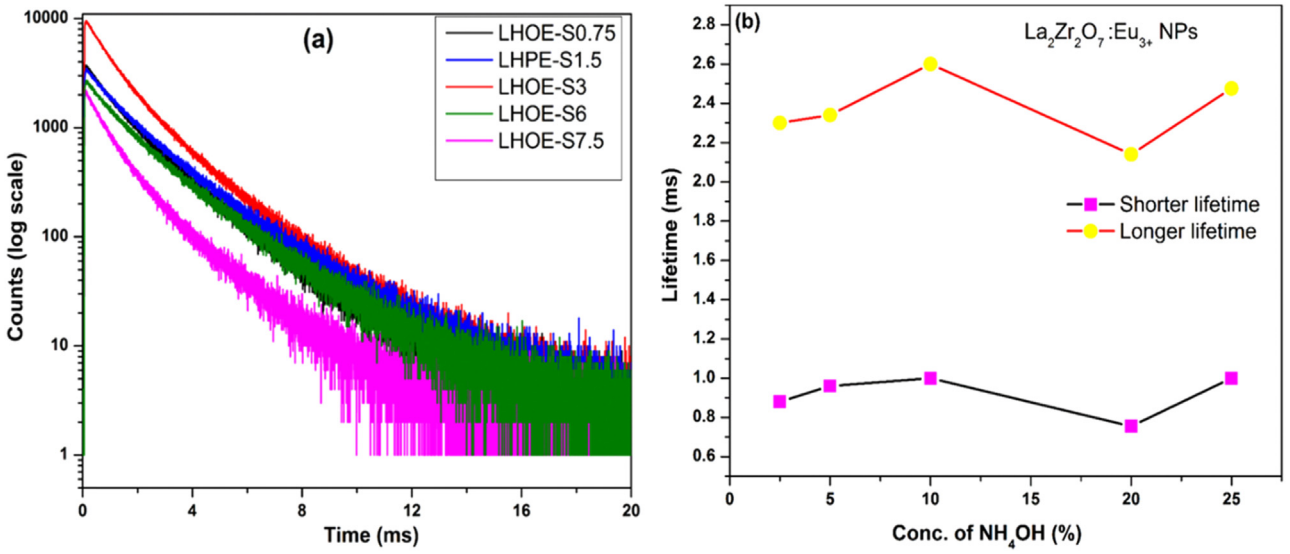

Fig. 10. (a) Luminescence decay profile of $^5D_0$ level of Eu^{3+} ions in the LZOE NPs under λ_{ex} = 276 nm and λ_{em} = 613 nm. (b) Variations of the lifetime value of the LZOE NPs as a function of the precipitating NH_4OH concentration.

Table 6
Radiative/non-radiative transition rate, internal quantum efficiency, J-O parameters and branching rations of the LZOE NPs.

Samples	A_R (s^{-1})	A_{NR} (s^{-1})	η (%)	Ω_2 (*10^{-20})	Ω_4 (*10^{-20})	β_1 (%)	β_2 (%)	β_3 (%)
LZOE-S0.75	384	237.5	61.8	2.83	1.53	13.0	56.8	15.1
LZOE-S1.5	354	267.4	54.1	2.86	1.57	14.9	65.5	17.7
LZOE-S3	336	284.9	47.4	2.41	1.39	17.0	63.0	17.9
LZOE-S6	294	326.8	53.5	3.12	1.51	14.1	67.9	16.2
LZOE-S7.5	333	288.2	56.9	2.83	1.55	15.0	65.4	17.7

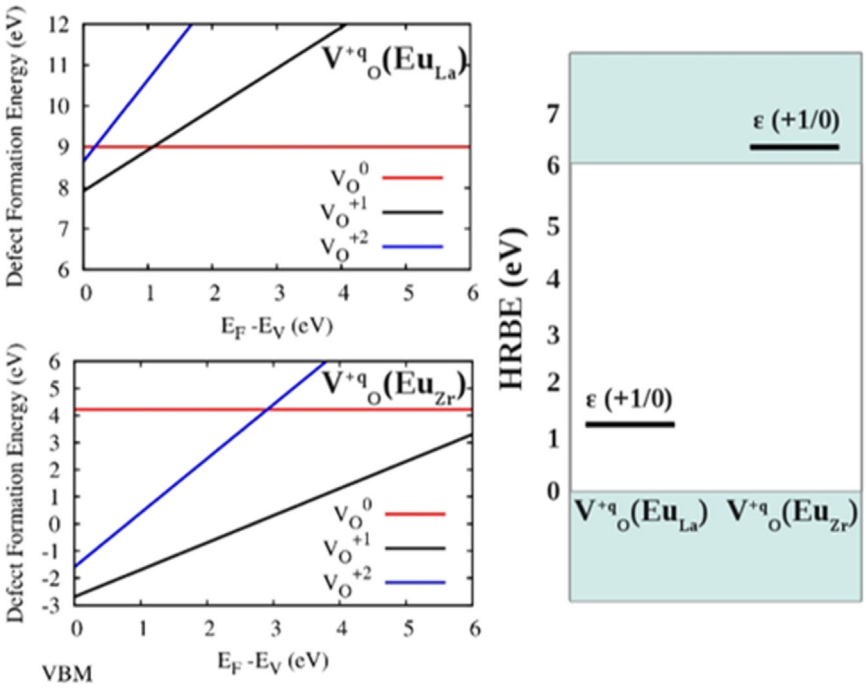

Fig. 11. GGA + U calculated oxygen defect formation energy (V_O^{+q}) versus Fermi level (E_F) for three charge states: q = 0, +1 and +2 in Eu-doped LZO at La site (Eu_{La}) and Zr site (Eu_{Zr}) (left panel). The defects exhibit one deep donor level $\varepsilon(+1/0)$ at 1.1 eV for Eu_{La} and another deep donor level $\varepsilon(+1/0)$ at 6.2 eV for Eu_{La} (left panel). The obtained impurity levels are shown in a conventional band diagram with respect to the host referred binding energies (HRBE) (right panel).

radiative pathways to quench fluorescence [2]. The larger the surface area, the large portion of Eu^{3+} ions located on or near the surface of the NPs which enhances the non-radiative probability. When these ions on the surface of NPs could be captured or reduced, their radiative transition probability will be increased. Furthermore, the effect of reduced agglomeration overpowers increased surface defect, therefore initial enhancement may be due to reduction in NPs aggregation as pH is increased. Aggregated particles scatter light and thus affect excited state population and the lifetime [78]. The LZOE-S3 sample displayed optimum crystalline feature in terms of defect and aggregation. Beyond that defect predominates and surface defect induced quenching takes place.

3.3.4. J-O analysis

Based on the J-O analysis, various photophysical parameters of the LZOE NPs are listed in Table 6. The phenomenon that non-radiative transition rate increases up to the LZOE-S6 NPs indicates the role of surface defect in fluorescence quenching at higher precipitation pH. The radiative transition rate is in line with QY and emission output as discussed above. The two most important J-O parameters (Ω_2 and Ω_4) give information about the nature of metal-oxygen bonding, local environment and polarizability. The fact that $\Omega_2 > \Omega_4$ from the LZOE NPs is an indication of the covalent character of interaction between the Eu^{3+} ions and the surrounding ligands [79]. Furthermore, the Ω_2 value increases progressively until the LZOE-S6 NPs, implying an increase of the extent of asymmetry around Eu^{3+} ions. The maximum asymmetric environment exists for the LZOE-S6 NPs, which is in line with asymmetry ratio calculated from emission spectra (Table 6). The internal quantum efficiency is also in agreement with the experimentally calculated values, which are well supported by the trend of the non-raditive transition probability. The branching ratio (β_s) indicating the maximum contribution to emission is β_2 for all LZOE NPs, which complement the intense red emission due to $^5D_0 \rightarrow {}^7F_2$ transition.

There is a limitation in Judd-Ofelt analysis of europium doped phosphor as we have used an average rarefactive index value. One should note that the values of quantum efficiency are slightly underestimated, since calculation does not account for $^5D_0 \rightarrow {}^7F_{3,5,6}$ emissions [80]. However, the trend of quantum efficiency change with the used pH for the synthesis of the $La_2Zr_2O_7$ nanoparticles is unaffected by this deficiency. Also, refraction index is wavelength dependent physical property, so taking the constant value into calculation introduces error into results. However, the error is small since the refractive index changes are small over the wavelength region of interest [81]. These simplifications are justified for the sake of comparison of J-O parameters and emission parameters among samples since the small errors cannot change the observed trends. It is acknowledged that Judd-Ofelt theory estimates transition probabilities with accuracy generally not worse than 10% [82].

Thermal quenching is an important property of rare earth doped phosphors. The activation energy of $La_2Zr_2O_7$:0.05Eu^{3+} phosphors was already reported by Min et al. [83] The activation energy was calculated to be 0.16 eV, indicating its outstanding thermal stability as a red emitting phosphor for WLEDs. On the other hand, for $La_2Hf_2O_7$:Eu^{3+} the activation energy was found to be 0.41 eV for thermal quenching [3], which is higher than the LZOE phosphors.

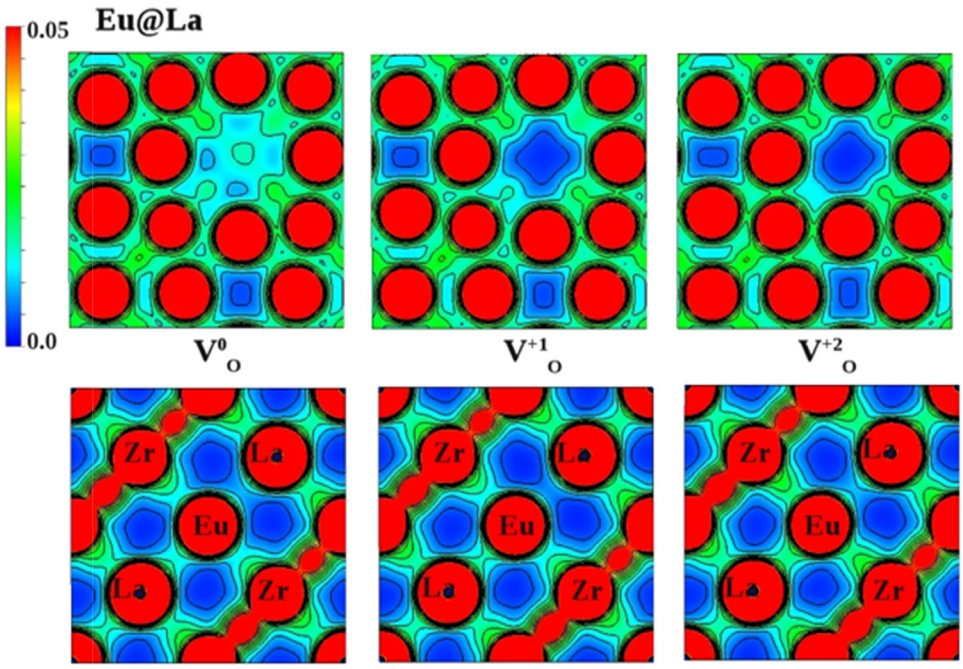

Fig. 12. Contour plots of valence charge density distribution ($e/Å^3$) on the atomic layer containing O vacancy (upper panel) and Eu atom (doped at La site). The atoms are oxygen atoms in the atomic layer containing oxygen vacancy.

3.4. Defect formation energies of LZOE with oxygen vacancy

To understand the observed luminescence properties of Eu^{3+} ions in the LZOE NPs, the cohesive energies of LZOE were calculated for Eu doping at La site and Zr site separately. To see how the defect formation energies of oxygen vacancies in LZO in the presence of Eu^{3+} doping in the dilute limit varies as a function of Fermi energy, we summarized the DFT calculated formation energies in Fig. 11 (left panel). The calculated vacancy formation energy values indicate that in the case of Eu^{3+} doping at La site, the formation of V_O^{+1} defect is favored at the 0–1.1 eV range (in E_F-E_V scale) near the valence band compared to V_O^{+2} and V_O^{0} oxygen defects, indicating that oxygen vacancies have a tendency to donate electrons. Similarly, the formation of V_O^{0} defects are favored in the 1.1–6 eV range (in E_F-E_V scale). On the contrary, the formation of V_O^{+1} defect is favorable throughout the energy range in the case of Eu doping at Zr site. Fig. 11 (right panel) shows that the defect exhibits two charge-state transition levels: a deep donor level $\varepsilon(+1/0)$ at 1.1 eV (for Eu@La case) and another deep donor level $\varepsilon(+1/0)$ at 6.2 eV (for Eu@Zr case). At this transition level, no emission spectra were found and hence we could not correlate it with the experimental data. This deficiency could be attributed to the band-gap prediction error using GGA/GGA + U.

Fig. 12 shows the contour plots of valence charge density distribution on the atomic layer containing O vacancy and Eu atom (doped at La site). It is evident from the figure that the valence charge density is localized at the oxygen vacancy site and not at the Eu^{3+} dopant site.

4. Conclusion

In this work, we successfully synthesized undoped and europium doped $La_2Zr_2O_7$ NPs at 650 °C using MSS. Interestingly, on UV irradiation, the undoped LZO NPs displayed blue and red emissions which was assigned to presence of oxygen vacancies in their band gap. In surge to make NPs with different sizes without subjecting them to high temperatures or long annealing time, coprecipitated precursors were prepared by changing the concentration of NH_4OH prior to the MSS step. It was observed that as the pH of the coprecipitation step was raised, the particle size of the LZO and LZOE NPs decreased. In addition, we observed a decrease in photoluminescence intensity, QY and RL with increasing coprecipitating pH due to the increase of surface defects. On doping europim ion, a complete transfer of energy from LZO host to Eu^{3+} dopant was observed, leading to efficient red emission in the LZOE NPs. The emission intensity progressively decreases as the pH increases up to LZOE-S6, after that there is a slight increase. Furthermore, Judd-Ofelt analysis indicated an increase in extent of asymmetry around europium ion. The maximum asymmetric environment was found for LZOE-S6. Lastly, DFT calculations showed that oxygen vacancies are responsible for violet-blue and red emissions in LZO NPs.

Acknowledgement

The authors thank the financial support by the National Science Foundation under CHE (award #1710160) and DMR (grant #1523577) and the USDA National Institute of Food and Agriculture (award #2015-38422-24059). The Department of Chemistry at the University of Texas Rio Grande Valley is grateful for the generous support provided by a Departmental Grant from the Robert A. Welch Foundation (Grant No. BX-0048). SKG thanks the United States-India Education Foundation (USIEF, India) and the Institute of International Education (IIE, USA) for his Fulbright Nehru Postdoctoral Fellowship (Award# 2268/FNPDR/2017).

References

[1] S.K. Gupta, K. Sudarshan, P. Ghosh, A. Srivastava, S. Bevara, P. Pujari, R. Kadam, Role of various defects in the photoluminescence characteristics of nanocrystalline $Nd_2Zr_2O_7$: an investigation through spectroscopic and DFT calculations, J. Mater. Chem. C 4 (2016) 4988–5000.

[2] S.K. Gupta, J.P. Zuniga, M. Abdou, Y. Mao, Thermal annealing effects on $La_2Hf_2O_7$:Eu^{3+} nanoparticles: a curious case study of structural evolution and site-specific photo- and radio-luminescence, Inorg. Chem. Front. 5 (2018) 2508–2521.

[3] S.K. Gupta, J.P. Zuniga, P.S. Ghosh, M. Abdou, Y. Mao, Correlating structure and luminescence properties of undoped and $La_2Hf_2O_7$:Eu^{3+} NPs prepared with different coprecipitating pH values through experimental and theoretical studies, Inorg. Chem. 57 (2018) 11815–11830.

[4] C. Kaliyaperumal, A. Sankarakumar, J. Palanisamy, T. Paramasivam, Fluorite to pyrochlore phase transformation in nanocrystalline $Nd_2Zr_2O_7$, Mater. Lett. 228 (2018) 493–496.

[5] J.P. Zuniga, S.K. Gupta, M. Abdou, Y. Mao, Effect of molten salt synthesis processing duration on the photo- and radioluminescence of UV-, visible-, and X-ray-excitable $La_2Hf_2O_7$:Eu^{3+} nanoparticles, ACS Omega 3 (2018) 7757–7770.

[6] J. Yang, Y. Han, M. Shahid, W. Pan, M. Zhao, W. Wu, C. Wan, A promising material for thermal barrier coating: pyrochlore-related compound Sm_2FeTaO_7, Scr. Mater.

149 (2018) 49–52.
[7] S.-K. Jian, W. Nie, Weyl magnons in pyrochlore antiferromagnets with an all-in-all-out order, Phys. Rev. B 97 (2018) 115162.
[8] T.M.H. Nguyen, L.J. Sandilands, C. Sohn, C. Kim, A.L. Wysocki, I.-S. Yang, S. Moon, J.-H. Ko, J. Yamaura, Z. Hiroi, Two-magnon scattering in the 5 d all-in-all-out pyrochlore magnet $Cd_2O_2O_7$, Nat. Commun. 8 (2017) 251.
[9] S. Urban, I. Djerdj, P. Dolcet, L. Chen, M. Mo¨ller, O. Khalid, H. Camuka, Rd Ellinghaus, C. Li, S. Gross, In situ study of the oxygen-induced transformation of pyrochlore $Ce_2Zr_2O_{7+x}$ to the κ-$Ce_2Zr_2O_8$ phase, Chem. Mater. 29 (2017) 9218–99226.
[10] N. Li, Y. Yin, F. Meng, Q. Zhang, J. Yan, Q. Jiang, Enabling pyrochlore-type oxides as highly efficient electrocatalysts for high-capacity and stable Na–O_2 batteries: the synergy of electronic structure and morphology, ACS Catal. 7 (2017) 7688–7694.
[11] F. Zhong, J. Zhao, L. Shi, Y. Xiao, G. Cai, Y. Zheng, J. Long, Alkaline-earth metals-doped pyrochlore $Gd_2Zr_2O_7$ as oxygen conductors for improved NO_2 sensing performance, Sci. Rep. 7 (2017) 4684.
[12] Y. Zhao, N. Li, C. Xu, Y. Li, H. Zhu, P. Zhu, X. Wang, W. Yang, Abnormal pressure-induced photoluminescence enhancement and phase decomposition in pyrochlore $La_2Sn_2O_7$, Adv. Mater. 29 (2017) 1701513.
[13] A.V. Shlyakhtina, K. Pygalskiy, D. Belov, N.V. Lyskov, E. Kharitonova, I. Kolbanev, A. Boruniova, O. Karyagina, E. Sadovskaya, V. Sadykov, Proton and oxygen ion conductivity in the pyrochlore/fluorite family of $Ln_{2-x}Ca_xScMO_{7-\delta}$ (Ln = La, Sm, Ho, Yb; M = Nb, Ta; x = 0, 0.05, 0.1) niobates and tantalates, Dalton Trans. 47 (2018) 2376–2392.
[14] R. Perriot, P.P. Dholabhai, B.P. Uberuaga, The role of surfaces, chemical interfaces, and disorder on plutonium incorporation in pyrochlores, Phys. Chem. Chem. Phys. 18 (2016) 22852–22863.
[15] R.S. Rejith, J.K. Thomas, S. Solomon, Structural, optical and impedance spectroscopic characterizations of $RE_2Zr_2O_7$ (RE = La, Y) ceramics, Solid State Ion. 323 (2018) 112–122.
[16] G.M. Mustafa, S. Atiq, S.K. Abbas, S. Riaz, S. Naseem, Tunable structural and electrical impedance properties of pyrochlores based Nd doped lanthanum zirconate nanoparticles for capacitive applications, Ceram. Int. 44 (2) (2018) 2170–2177.
[17] A. Jamil, J. Schläfer, Y. Gönüllü, A. Lepcha, S. Mathur, Precursor-derived rare earth metal pyrochlores: $Nd_2Sn_2O_7$ nanofibers and thin films as efficient photoabsorbers, Cryst. Growth Des. 16 (2016) 5260–5267.
[18] S. Zinatloo-Ajabshir, Z. Salehi, M. Salavati-Niasari, Green synthesis and characterization of $Dy_2Ce_2O_7$ nanostructures using Ananas comosus with high visible-light photocatalytic activity of organic contaminants, J. Alloy. Compd. 763 (2018) 314–321.
[19] M.G. Nikolic, M.S. Rabasovic, J. Krizan, S. Savic-Sevic, M.D. Rabasovic, B.P. Marinkovic, A. Vlasic, D. Sevic, Luminescence thermometry using $Gd_2Zr_2O_7$:Eu3+, Opt. Quant. Elctron. 50 (6) (2018) 258.
[20] R. Zhu, J. Zou, D. Wang, K. Zou, D. Gao, J. Mao, M. Liu, X-ray diffractional, spectroscopic and thermo-physical properties analyses on Eu-doped lanthanum zirconate ceramic for thermal barrier coatings, J. Alloy. Compd. 746 (2018) 62–67.
[21] J.P. Zuniga, S.K. Gupta, M. Pokhrel, Y. Mao, Exploring the optical properties of $La_2Hf_2O_7$:Pr^{3+} nanoparticles under UV and X-ray excitation for potential lighting and scintillating applications, New J. Chem. 42 (2018) 9381–9392.
[22] M. Abdou, S.K. Gupta, J.P. Zuniga, Y. Mao, On structure and phase transformation of uranium doped $La_2Hf_2O_7$ nanoparticles as an efficient nuclear waste host, Mater. Chem. Front. 2 (2018) 2201–2211.
[23] M. Pokhrel, K. Wahid, Y. Mao, Systematic studies on $RE_2Hf_2O_7$:5% Eu^{3+} (RE = Y, La, Pr, Gd, Er, and Lu) nanoparticles: effects of the A-site RE^{3+} cation and calcination on structure and photoluminescence, J. Phys. Chem. C 27 (2016) 14828–14839.
[24] M. Pokhrel, M. Alcoutlabi, Y. Mao, Optical and X-ray induced luminescence from Eu^{3+} doped $La_2Zr_2O_7$ nanoparticles, J. Alloy. Compd. 693 (2017) 719–729.
[25] J.P. Zuniga, S.K. Gupta, M. Pokhrel, Y. Mao, Exploring optical properties of $La_2Hf_2O_7$:Pr^{3+} nanoparticles under UV and X-ray excitations for potential lighting and scintillating applications, New J. Chem. 42 (2018) 9381–9392.
[26] K. Wahid, M. Pokhrel, Y. Mao, Structural, photoluminescence and radioluminescence properties of Eu^{3+} doped $La_2Hf_2O_7$ nanoparticles, J. Solid State Chem. 245 (2017) 89–97.
[27] A. Juyal, A. Agarwal, S. Mukhopadhyay, Negative Longitudinal Magnetoresistance in the Density Wave Phase of $Y_2Ir_2O_7$, Phys. Rev. Lett. 120 (9) (2018) 096801.
[28] S. Saitzek, Z. Shao, A. Bayart, A. Ferri, M. Huvé, P. Roussel, R. Desfeux, Ferroelectricity in $La_2Zr_2O_7$ thin films with a frustrated pyrochlore-type structure, J. Mater. Chem. C 2 (2014) 4037–4043.
[29] F. Zhang, M. Lang, Z. Liu, R. Ewing, Pressure-induced disordering and anomalous lattice expansion in $La_2Zr_2O_7$ pyrochlore, Phys. Rev. Lett. 105 (2010) 015503.
[30] N.M. Sangeetha, F.C. van Veggel, Lanthanum silicate and lanthanum zirconate nanoparticles co-doped with Ho^{3+} and Yb^{3+}: matrix-dependent red and green upconversion emissions, J. Phys. Chem. C 113 (2009) 14702–14707.
[31] A. Srivastava, W. Beers, On the impurity trapped exciton luminescence in $La_2Zr_2O_7$:Bi^{3+}, J. Lumin. 81 (1999) 293–300.
[32] M. Pokhrel, A. Burger, M. Groza, Y. Mao, Enhance the photoluminescence and radioluminescence of La2Zr2O7:Eu3+ core nanoparticles by coating with a thin Y2O3 shell, Opt. Mater. 68 (2017) 35–41.
[33] M. Pokhrel, M.G. Brik, Y. Mao, Particle size and crystal phase dependent photoluminescence of $La_2Zr_2O_7$:Eu^{3+} nanoparticles, J. Am. Ceram. Soc. 98 (2015) 3192–3201.
[34] R. Liu, X. Dong, J. Wang, W. Yu, G. Liu, Preparation, characterization and luminescence properties of pyrochlore $La_2Zr_2O_7$:Eu^{3+} nanofibers by electrospinning, J. Optoelectron. Adv. Mater. 16 (2014) 542–546.
[35] S.B. Alaparthi, Y. Tian, Y. Mao, Synthesis and photoluminescence properties of $La_2Zr_2O_7$:Eu^{3+}@YBO_3 core@ shell nanoparticles, Nanotechnology 25 (2013) 025703.
[36] S.K. Gupta, P.S. Ghosh, A.K. Yadav, N. Pathak, A. Arya, S.N. Jha, D. Bhattacharyya, R.M. Kadam, Luminescence properties of $SrZrO_3$/Tb^{3+} perovskite: host-dopant energy-transfer dynamics and local structure of Tb^{3+}, Inorg. Chem. 55 (2016) 1728–1740.
[37] S.K. Gupta, M. Sahu, P.S. Ghosh, D. Tyagi, M.K. Saxena, R.M. Kadam, Energy transfer dynamics and luminescence properties of Eu^{3+} in $CaMoO_4$ and $SrMoO_4$, Dalton Trans. 44 (2015) 18957–18969.
[38] S.K. Gupta, P.S. Ghosh, A.K. Yadav, S.N. Jha, D. Bhattacharyya, R.M. Kadam, Origin of Blue-Green Emission in α-$Zn_2P_2O_7$ and Local Structure of Ln^{3+} Ion in α-$Zn_2P_2O_7$:Ln^{3+} (Ln = Sm, Eu): time-resolved Photoluminescence, EXAFS, and DFT Measurements, Inorg. Chem. 56 (2017) 167–178.
[39] S.K. Gupta, V. Grover, R. Shukla, K. Srinivasu, V. Natarajan, A.K. Tyagi, Exploring pure and RE co-doped (Eu^{3+}, Tb^{3+} and Dy^{3+}) gadolinium scandate: luminescence behaviour and dynamics of energy transfer, Chem. Eng. J. 283 (2016) 114–126.
[40] S.K. Gupta, P.S. Ghosh, A.K. Yadav, S.N. Jha, D. Bhattacharyya, R.M. Kadam, Origin of blue-green emission in α-$Zn_2P_2O_7$ and local structure of Ln^{3+} Ion in α-$Zn_2P_2O_7$:Ln (Ln = Sm, Eu): time-resolved photoluminescence, EXAFS, and DFT measurements, Inorg. Chem. 56 (2016) 167–178.
[41] J.P. Zuniga, M. Abdou, S.K. Gupta, Y. Mao, Molten-Salt Synthesis of Complex Metal Oxide Nanoparticles, JoVE 140 (2018) e58482.
[42] E.S. Larsen, H. Berman, The Microscopic Determination of the Nonopaque Minerals, US Government Printing Office, 1934.
[43] W. Carnall, P. Fields, K. Rajnak, Spectral intensities of the trivalent lanthanides and actinides in solution. II. Pm^{3+}, Sm^{3+}, Eu^{3+}, Gd^{3+}, Tb^{3+}, Dy^{3+}, and Ho^{3+}, J. Chem. Phys. 49 (1968) 4412–4423.
[44] W. Carnall, H. Crosswhite, H.M. Crosswhite, Energy Level Structure and Transition Probabilities in the Spectra of the Trivalent Lanthanides in LaF_3, Argonne National Lab.(ANL), Argonne, IL (United States), 1978.
[45] S.J. Ribeiro, R. Diniz, Y. Messaddeq, L.A. Nunes, M.A. Aegerter, Eu^{3+} and Gd^{3+} spectroscopy in fluoroindate glasses, Chem. Phys. Lett. 220 (1994) 214–218.
[46] M.H. Werts, R.T. Jukes, J.W. Verhoeven, The emission spectrum and the radiative lifetime of Eu^{3+} in luminescent lanthanide complexes, Phys. Chem. Chem. Phys. 4 (2002) 1542–1548.
[47] S. Dudarev, G. Botton, S. Savrasov, C. Humphreys, A. Sutton, Electron-energy-loss spectra and the structural stability of nickel oxide: an LSDA+ U study, Phys. Rev. B 57 (3) (1998) 1505.
[48] D. Richard, E.L. Muñoz, M. Rentería, L.A. Errico, A. Svane, N.E. Christensen, Abinitio LSDA and LSDA+ U study of pure and Cd-doped cubic lanthanide sesquioxides, Phys. Rev. B 88 (16) (2013) 165206.
[49] G. Kresse, J. Furthmüller, Efficiency of ab-initio total energy calculations for metals and semiconductors using a plane-wave basis set, Comput. Mater. Sci. 6 (1996) 15–50.
[50] G. Kresse, J. Furthmüller, Efficient iterative schemes for ab initio total-energy calculations using a plane-wave basis set, Phys. Rev. B 54 (16) (1996) 11169.
[51] P.E. Blöchl, Projector augmented-wave method, Phys. Rev. B 50 (1994) 17953.
[52] J.P. Perdew, K. Burke, M. Ernzerhof, Generalized gradient approximation made simple, Phys. Rev. Lett. 77 (1996) 3865.
[53] H.J. Monkhorst, J.D. Pack, Special points for Brillouin-zone integrations, Phys. Rev. B 13 (12) (1976) 5188.
[54] P.E. Blöchl, O. Jepsen, O.K. Andersen, Improved tetrahedron method for Brillouin-zone integrations, Phys. Rev. B 49 (23) (1994) 16223.
[55] M. Marsman, J. Paier, A. Stroppa, G. Kresse, Hybrid functionals applied to extended systems, J. Phys.: Condens. Matter 20 (2008) 064201.
[56] M. Tsega, F. Dejene, Influence of acidic pH on the formulation of TiO_2 nanocrystalline powders with enhanced photoluminescence property, Heliyon 3 (2017) e00246.
[57] Y. Li, J. Zhang, X. Zhang, Y. Luo, X. Ren, H. Zhao, X. Wang, L. Sun, C. Yan, Near-infrared to visible upconversion in Er^{3+} and Yb^{3+} codoped Lu_2O_3 nanocrystals: enhanced red color upconversion and three-photon process in green color upconversion, J. Phys. Chem. C 113 (2009) 4413–4418.
[58] K. Swaroop, H. Somashekarappa, Effect of pH values on surface morphology and particle size variation in ZnO nanoparticles synthesised by co-precipitation method, Res. J. Recent Sci. 2277 (2015) 2502.
[59] K. Wahid, M. Pokhrel, Y. Mao, Structural, photoluminescence and radioluminescence properties of Eu^{3+} doped $La_2Hf_2O_7$ nanoparticles, J. Solid State Chem. 245 (2017) 89–97.
[60] V.V. Popov, A.P. Menushenkov, A.A. Yaroslavtsev, Y.V. Zubavichus, B.R. Gaynanov, A.A. Yastrebtsev, D.S. Leshchev, R.V. Chernikov, Fluorite-pyrochlore phase transition in nanostructured $Ln_2Hf_2O_7$ (Ln = La-Lu), J. Alloy. Compd. 689 (2016) 669–679.
[61] X. Wang, Y. Zhu, W. Zhang, Preparation of lanthanum zirconate nano-powders by Molten Salt method, J. Non-Cryst. Solids 356 (20–22) (2010) 1049–1051.
[62] M. Subramanian, G. Aravamudan, G.S. Rao, Oxide pyrochlores—a review, Prog. Solid State Chem. 15 (1983) 55–143.
[63] Y. Tabira, R.L. Withers, L. Minervini, R.W. Grimes, Systematic structural change in selected rare earth oxide pyrochlores as determined by wide-angle CBED and a comparison with the results of atomistic computer simulation, J. Solid State Chem. 153 (2000) 16–25.
[64] B. Liu, J. Wang, Y. Zhou, T. Liao, F. Li, Theoretical elastic stiffness, structure stability and thermal conductivity of La2Zr2O7 pyrochlore, Acta Mater. 55 (9) (2007) 2949–2957.
[65] J. Liang, Z. Deng, X. Jiang, F. Li, Y. Li, Photoluminescence of tetragonal ZrO_2 nanoparticles synthesized by microwave irradiation, Inorg. Chem. 41 (2002)

3602–3604.
[66] S.K. Gupta, P. Ghosh, C. Reghukumar, N. Pathak, R. Kadam, Experimental and theoretical approach to account for green luminescence from $Gd_2Zr_2O_7$ pyrochlore: exploring the site occupancy and origin of host-dopant energy transfer in $Gd_2Zr_2O_7$:Eu^{3+}, RSC Adv. 6 (2016) 44908–44920.
[67] M. Leslie, N. Gillan, The energy and elastic dipole tensor of defects in ionic crystals calculated by the supercell method, J. Phys. C: Solid State Phys. 18 (5) (1985) 973.
[68] X. Cheng, Z. Qi, T. Li, G. Zhang, C. Li, H. Zhou, Y. Wang, M. Yin, Infrared phonon modes and dielectric properties of $La_2Zr_2O_7$: comparing thin film to bulk material, Phys. Status Solidi (b) 249 (4) (2012) 854–857.
[69] J.P. Zuniga, S.K. Gupta, M. Abdou, Y. Mao, Effect of molten salt synthesis processing duration on the photo- and radioluminescence of UV-, visible-, and X-ray-excitable $Gd_2Hf_2O_7$:Eu^{3+} nanoparticles, ACS Omega 3 (7) (2018) 7757–7770.
[70] M. Pokhrel, K. Wahid, Y. Mao, Systematic studies on $RE_2Hf_2O_7$:5% Eu^{3+} (RE= Y, La, Pr, Gd, Er, and Lu) nanoparticles: effects of the A-site RE^{3+} cation and calcination on structure and photoluminescence, J. Phys. Chem. C 120 (2016) 14828–14839.
[71] S.K. Gupta, C. Reghukumar, R. Kadam, Eu^{3+} local site analysis and emission characteristics of novel $Nd_2Zr_2O_7$:Eu phosphor: insight into the effect of europium concentration on its photoluminescence properties, RSC Adv. 6 (2016) 53614–53624.
[72] S.K. Gupta, P.S. Ghosh, C. Reghukumar, N. Pathak, R.M. Kadam, Experimental and theoretical approach to account for green luminescence from $Gd_2Zr_2O_7$ pyrochlore: exploring the site occupancy and origin of host-dopant energy transfer in $Gd_2Zr_2O_7$:Eu^{3+}, RSC Adv. 6 (50) (2016) 44908–44920.
[73] S.K. Gupta, C. Reghukumar, K. Sudarshan, P.S. Ghosh, N. Pathak, R.M. Kadam, Orange-red emitting $Gd_2Zr_2O_7$:Sm^{3+}: structure-property correlation, optical properties and defect spectroscopy, J. Phys. Chem. Solids 116 (2018) 360–366.
[74] S.K. Gupta, P.S. Ghosh, A.K. Yadav, S.N. Jha, D. Bhattacharyya, R.M. Kadam, Origin of blue-green emission in α-$Zn_2P_2O_7$ and local structure of Ln^{3+} ion in α-$Zn_2P_2O_7$:Ln^{3+} (Ln= Sm, Eu): time-resolved photoluminescence, EXAFS, and DFT measurements, Inorg. Chem. 56 (2016) 167–178.
[75] S.K. Gupta, P.S. Ghosh, A.K. Yadav, N. Pathak, A. Arya, S.N. Jha, D. Bhattacharyya, R.M. Kadam, Luminescence properties of $SrZrO_3$/Tb^{3+} perovskite: host-dopant energy-transfer dynamics and local structure of Tb^{3+}, Inorg. Chem. 55 (2016) 1728–1740.
[76] S.K. Gupta, M. Mohapatra, S. Godbole, V. Natarajan, On the unusual photoluminescence of Eu^{3+} in α-$Zn_2P_2O_7$: a time resolved emission spectrometric and Judd–Ofelt study, RSC Adv. 3 (43) (2013) 20046–20053.
[77] S.K. Gupta, M. Sahu, K. Krishnan, M. Saxena, V. Natarajan, S. Godbole, Bluish white emitting Sr2CeO4 and red emitting Sr2CeO4:Eu3+ nanoparticles: optimization of synthesis parameters, characterization, energy transfer and photoluminescence, J. Mater. Chem. C 1 (42) (2013) 7054–7063.
[78] W.-N. Wang, W. Widiyastuti, T. Ogi, I.W. Lenggoro, K. Okuyama, Correlations between crystallite/particle size and photoluminescence properties of submicrometer phosphors, Chem. Mater. 19 (7) (2007) 1723–1730.
[79] M. Gökçe, U. Şentürk, D.K. Uslu, G. Burgaz, Y. Şahin, A.G. Gökçe, Investigation of europium concentration dependence on the luminescent properties of borogermanate glasses, J. Lumin. 192 (2017) 263–268.
[80] K. Vukovic, M. Medic, Milica Sekulić, M.D. Dramićanin, Analysis of Eu^{3+} emission from Mg_2TiO_4 nanoparticles by Judd-Ofelt theory, Condens. Matter Phys. 2015 (2015) 7.
[81] L. Đačanin, S. Lukić, D. Petrović, M. Nikolić, M. Dramićanin, Judd–Ofelt analysis of luminescence emission from Zn_2SiO_4:Eu^{3+} nanoparticles obtained by a polymer-assisted sol–gel method, Phys. B: Condens. Matter 406 (11) (2011) 2319–2322.
[82] R. Rolli, K. Gatterer, M. Wachtler, M. Bettinelli, A. Speghini, D. Ajo, Optical spectroscopy of lanthanide ions in ZnO–TeO_2 glasses, Spectrochim. Acta Part A: Mol. Biomol. Spectrosc. 57 (10) (2001) 2009–2017.
[83] X. Min, Y. Sun, L. Kong, M. Guan, M. Fang, Yg Liu, X. Wu, Z. Huang, Novel pyrochlore-type $La_2Zr_2O_7$:Eu^{3+} red phosphors: synthesis, structural, luminescence properties and theoretical calculation, Dyes Pigments 157 (2018) 47–54.